Ensemble-based Sensitivity Analysis applied to African Easterly Waves

Ryan D. Torn *

National Center for Atmospheric Research†, Boulder, CO and

Department of Earth and Atmospheric Sciences, University at Albany, State University of New York, Albany, NY

* *Corresponding author address:* Ryan Torn, University at Albany, State University of New York, DEAS-ES 351, 1400 Washington Avenue, Albany, NY 12222.

E-mail: torn@atmos.albany.edu

†The National Center for Atmospheric Research is supported by the National Science Foundation

ABSTRACT

An ensemble Kalman filter (EnKF) coupled to the Advanced Research version of the Weather Research and Forecasting (WRF) model is used to generate ensemble analyes and forecasts of a strong African Easterly Wave (AEW) during the African Monsoon Multidisciplinary Analysis field campaign. Ensemble sensitivity analysis is then used to evaluate the impact of initial condition errors on AEW amplitude and position forecasts at two different initialization times.

WRF forecasts initialized at 0000 UTC 8 September 2006 prior to the amplification of the AEW are characterized by large ensemble variance as compared to forecasts initialized 48 hours later when the AEW is within a denser observation network. Short lead time amplitude forecasts are most sensitive to the mid-tropospheric meridional winds and the mid-tropospheric θ_e, while at longer lead times, mid-tropospheric θ_e errors have a larger impact. For AEW longitude forecasts, the largest sensitivities are associated with the θ_e downstream of the AEW, and to a lesser extent, the meridional winds. Ensemble predictions of initial condition errors impact the AEW amplitude and position compare qualitatively well with perturbed integrations of the WRF model.

Much of the precipitation associated with the AEW is generated by the Kain-Fritsch cumulus parameterization, thus the initial-condition sensitivities are also computed for ensemble forecasts that use the Betts-Miller-Janjic and Grell cumulus parameterization scheme, and a high-resolution nested domain with explicit convection. While the 12 hour AEW amplitude forecast is characterized by consistent initial-condition sensitivity among the different schemes, there is more variability beyond 24 hours. In contrast, the AEW position forecast is sensitive to the downstream thermodynamic profile regardless of cumulus scheme.

1. Introduction

African Easterly Waves (AEWs) are synoptic-scale waves that propagate westward through the sub-Sahara Africa during the Northern Hemisphere summer (Burpee 1972). These waves are important to this region because they provide a significant fraction of seasonal rainfall and are often associated with mesoscale convective systems (e.g., Payne and McGarry 1977; Fink and Reiner 2003). Once over the Atlantic ocean, AEW also provide seed disturbances for tropical cyclones (Avila and Pasch 1992).

Much of the work to date has focused on understanding the structure, dynamics and growth mechanisms of these features. In general, AEW are characterized by a periodicity between 2-5 days (Burpee 1972) and have amplitudes that are peaked at around 650 hPa (Reed et al. 1977). Composite AEW studies and idealized models indicate that AEW grow via baroclinc and barotropic conversion processes in the region of the African Easterly Jet (e.g., Reed et al. 1977; Thorncroft and Hoskins 1994). More recent studies have emphasized the importance of diabatic processes linked to deep convection associated with the waves (Berry and Thorncroft 2005; Hsieh and Cook 2007).

Numerical Weather Prediction (NWP) model forecasts of AEWs suffer from a number of problems related to errors in the initial conditions and model formulations. Much of North Africa is characterized by a lack of in situ observations, thus many NWP systems rely on remote sensing data and prior forecasts to generate an analysis in this area (e.g., Tompkins et al. 2005). Furthermore, the relationship between diabatic heating, large-scale convection, and AEW suggest that the formulation of the convective parameterization plays a significant role in the model evolution. Berry et al. (2008) evaluated the skill of AEW

forecasts within four different operational NWP systems during 2007. Although the modeling systems had analyses over West Africa that were indistinguishable with respect to rawinsonde observations, short-term forecasts of AEW were characterized by varying degrees of skill. These operational systems use different initial conditions and physics parameterizations, thus it is difficult to determine the role of initial condition and model errors.

This paper explores how initial condition errors affect NWP model forecasts of AEW using forecast sensitivity analysis. Specifically, this study uses ensemble analysis and forecast data from a cycling ensemble Kalman filter (EnKF) system to compute the sensitivity of AEW metrics to initial conditions via ensemble-based sensitivity analysis (Hakim and Torn 2008). This work focuses on forecasts of an unusually strong AEW during the African Monsoon Multidisciplinary Analyses (AMMA) field campaign (Redelsperger et al. 2006), which provided an unusually rich set of observations over West Africa.

The paper is organized as follows. Section 2 gives details on the data assimilation system and model. An overview of the two forecasts studied is given in section 3. The sensitivity of the AEW forecasts to the initial conditions is presented in section 4, while in section 5, perturbations are added to the initial conditions in the most sensitive regions. In section 6, the role of the cumulus parameterization in the sensitivity results is investigated. A concluding summary is given in section 7.

2. Experiment Setup

Ensemble analyses of Northern Africa from 0000 UTC 1 September 2006 to 0000 UTC 1 October 2006 are generated each six-hours by cycling an EnKF system on a 36 km hori-

zontal resolution grid. Figure 1 shows the computational domain for these experiments. The 96-member analysis ensemble is advanced in time using version 2.2.1 of the Advanced Research (ARW) version of the Weather Research and Forecasting (WRF) model (Skamarock et al. 2005). This implementation of WRF uses the WRF 3-class microphysics scheme (Hong et al. 2004), Kain-Fritsch (KF) cumulus parameterization (Kain and Fritsch 1990), Yonsei University (YSU) boundary-layer scheme (Hong et al. 2006) and similarity theory land surface model (Skamarock et al. 2005).

Wind, temperature, specific humidity and surface pressure observations are assimilated each six hours from surface stations, buoys, ships, rawinsondes including data taken during the AMMA field campaign, Aircraft Communications Addressing and Reporting System (ACARS), and cloud motion vectors (Velden et al. 2005) every six hours using the Data Assimilation Research Testbed (DART) (Anderson et al. 2008), which is an implementation of the Ensemble Adjustment Kalman Filter (Anderson 2001). A majority of the observations are along the western coast of Africa (Fig. 1); at a typical analysis time, roughly 5000 observations are assimilated. Observation errors are obtained from National Centers for Environmental Prediction (NCEP) operational data.

Approximating covariances via small ensembles tends to produce spurious long-distance covariances and underestimate the ensemble variance. These problems are partially overcome via covariance localization and covariance inflation. The influence of observations is limited using the Gaspari and Cohn (1999) localization function (their eqn. 4.10), where the covariance magnitude reduces to zero 2500 km (700 hPa) in the horizontal (vertical) from the observation location. The horizontal localization scale is obtained from Torn and Hakim (2008b), while the vertical localization scale is determined by repeating the cycling experi-

ments with varying localization values and comparing the resulting six-hour forecasts errors (computed with respect to rawinsondes). At each analysis time, the deviations from the ensemble mean are inflated using the spatially-adaptive inflation scheme of Anderson (2008) without inflation damping and an inflation standard deviation of 0.1; after approximately five days, the inflation factor becomes stable in time.

Ensemble initial and boundary conditions for this North Africa domain are taken from a comparable parent ensemble data assimilation system cycled on a larger domain. This parent ensemble has 108 km horizontal resolution and extends from the western United States to India and Northern Europe to South Africa and has all the same parameterization schemes as the Africa domain. The parent ensemble assimilates observations each six hours from 0000 UTC 10 August 2006 to 0000 UTC 1 October 2006 using the same observation types, covariance inflation and covariance localization setup as is used for the North Africa domain. One-way lateral boundary conditions for each North Africa domain ensemble member are obtained by interpolating the corresponding forecasts from a parent ensemble member onto the North Africa domain boundary points. Moreover, the North Africa ensemble is initialized on 0000 UTC 1 September 2006 by pairing each member with a parent domain analysis member and interpolating onto the North Africa grid.

For analysis times when AEW exist over West Africa, 48-hour ensemble forecasts are generated by integrating all 96 analysis ensemble members forward in time each 24 hours at 0000 UTC; for brevity, this study focuses on two different initialization times, which are described in the next section. Other initialization times gave qualitatively similar results in terms of forecast performance and initial condition sensitivity. Lateral boundary conditions for these ensemble forecasts are obtained by interpolating the corresponding time parent

ensemble forecast onto the North Africa domain.

3. Overview of Wave

Before evaluating how initial condition errors affect forecasts of AEW at two different times, a short summary of this system and the forecasts is presented. This AEW, one of the most vigorous observed during AMMA, is first identified by the Berry et al. (2007) objective tracking algorithm over southern Sudan at 0000 UTC 5 September 2006 (Thorncroft et al. 2007). Beginning 9 September, 700 hPa curvature vorticity associated with the AEW markedly increases as it moves into Western Africa. Once over Burkina Faso, several convective developments are observed in association with this AEW (e.g., Arnault and Roux 2008). At 0000 UTC 14 September (36 hours after moving off the African coast), the AEW is classified as Tropical Storm Helene by the National Hurricane Center (Brown 2006).

Forecasts of this AEW at two different points in its lifecycle are chosen for investigation, just prior to amplification on 0000 UTC 8 September (hereafter 8Sept), and during the mature stage starting 0000 UTC 10 September (hereafter 10Sept). Figure 2 shows the WRF EnKF ensemble-mean and standard deviation 700 hPa curvature vorticity as a function of forecast hour. At the initial time, the AEW is located over Nigeria and is characterized by ensemble mean curvature vorticity values of 1×10^{-5} sec^{-1} with a standard deviation of 0.7×10^{-5} sec^{-1}, which indicates that each member has varied AEW structures and positions, possibly due to the lack of observations in this region (c.f. Fig. 1). During subsequent forecast times, some of the ensemble members have the correct westward propagation and amplification, while others predict a stationary, or even dissipating system. As a conse-

quence, the 48-hour ensemble-mean curvature vorticity forecast does not have a definitive maximum, while the ensemble standard deviation exceeds 1.2 $\times 10^{-5}$ sec^{-1} (Fig. 2c). In general, the ensemble-mean precipitation is higher on the southwest side of the maximum in curvature vorticity standard deviation. The larger precipitation and vorticity standard deviation results from some, but not all members having an accurate forecast of the AEW.

In contrast to above, the 10Sept forecast has less variability among ensemble members. At the analysis time, the ensemble-mean curvature vorticity associated with the AEW (located over Burkina Faso) exceeds 2×10^{-5} sec^{-1}, while the standard deviation is less than 0.5×10^{-5} sec^{-1} (Fig. 2d). By hour 48, the AEW moves into eastern Senegal and the standard deviation increases to 0.9×10^{-5} sec^{-1} resulting from differences in the AEW position (Fig. 2f). At both forecast times, the ensemble-mean precipitation is greater than 8 mm per 6 hours over a large area on the south and west side of the AEW. The cumulus parameterization is responsible for greater than 90% of the precipitation; the implications of this will be addressed in section 6.

4. Forecast Sensitivities

The role of initial condition errors on these two AEW forecasts is quantified using ensemble analysis and forecast data. Here the sensitivity of a forecast metric J to a state variable x_i is evaluated from an M member ensemble via

$$\frac{\partial J}{\partial x_i} = \frac{cov(\mathbf{J}, \mathbf{x}_i)}{var(\mathbf{x}_i)} \sigma_{x_i}, \tag{1}$$

where $\mathbf{J}$ and $\mathbf{x}_i$ are $1 \times M$ ensemble estimates of the forecast metric and ith state variable, respectively, σ_{x_i} is the analysis standard deviation of this state variable, *cov* denotes the covariance between the two arguments, and *var* is the variance (Ancell and Hakim 2007). This equation is a linear regression between the analysis state variable and forecast metric, which are the independent and dependent variables, respectively. Multiplying the right hand side by the ensemble standard deviation, which is an approximation of the analysis error, allows for a qualitative comparison between forecast hours and fields. Ensemble sensitivity is estimated from a relatively small ensemble compared to the number of state variables, thus the regression coefficient is subject to sampling errors, which are addressed by testing for statistical significance in a manner similar to Torn and Hakim (2008a). In particular, the null hypothesis of no relationship between the metric and analysis state variable is rejected if the absolute value of the regression coefficient is greater than its 95% confidence bounds computed from ensemble data (e.g., Wilks 2005, section 6.2.5).

Initial condition sensitivity is evaluated for two different metrics related to AEW, the 700 hPa meridional wind kinetic energy in the vicinity of the AEW, and the longitude of the AEW. The meridional wind kinetic energy (MKE), which is used as a proxy for the AEW amplitude, is computed for each ensemble member by averaging the kinetic energy associated with the 700 hPa meridional wind over a box centered on the ensemble-mean AEW position. For the AEW longitude, the 700 hPa curvature vorticity is computed for each member using the Berry et al. (2007) technique, with the exception that the vorticity is computed from the full wind at 700 hPa. The AEW longitude is found by averaging the curvature vorticity between 8 °N and 18 °N latitude at each grid point in the x direction and finding the longitude of the maximum value. Sensitivities for 700 hPa curvature vorticity

averaged over a box centered on the ensemble-mean AEW showed statistically insignificant sensitivities, thus this metric is not considered.

Given that AEWs have maximum amplitude in the mid-troposphere and the role of diabatic processes in their evolution, the sensitivity of 12 and 48 hour MKE forecasts is computed with respect to the analysis of the 700 hPa meridional wind and the equivalent potential temperature (θ_e) averaged between 3000 and 7000 m. Although θ_e is not a WRF state variable, this field allows for a quantitative comparison of the role of thermodynamic errors versus kinematic errors. In general, locations that are sensitive to θ_e are sensitive to both the temperature and moisture at that location (not shown). Other fields, such as zonal winds or lower tropospheric fields, are characterized by minimal or statistically insignificant sensitivities (not shown).

a. Meridional Kinetic Energy

For 8Sept, the regions of largest sensitivity for the 12 hour MKE forecast are co-located with the meridional wind maxima associated with the AEW over Nigeria (Fig. 3a). Increasing (decreasing) the southerly (northerly) merdional winds on the eastern (western) side of the AEW by one standard deviation is associated with a 2 m^2 sec^{-2} increase in the 12 hour meridional kinetic energy, which is equivalent to a 0.5 standard deviation change in this metric (see Fig. 2a for initial AEW position). This pattern of sensitivity suggests that short-term forecasts have memory of the initial AEW amplitude. In contrast, the region of maximum sensitivity to mid-tropospheric θ_e is on the north-eastern side of the AEW and is comparatively smaller (1.5 m^2 sec^{-2} per analysis standard deviation) than the meridional

wind value (Fig. 3b). This region of sensitivity is nearly co-located with the Jos Plateau; the implications of this will be discussed later.

The region of large initial-condition sensitivity is not just limited to the mid-troposphere. Fig. 4 shows the vertical profile of the sensitivity to the meridional winds and θ_e within the area of maximum sensitivity (denoted by dots in Fig. 3a,b). The initial condition sensitivity is nonzero between 2-6 km, which roughly coincides with the strongest northerly winds; above and below these levels, the ensemble sensitivity is statistically insignificant (Fig. 4a). In contrast, the sensitivity for θ_e is statistically significant from 2 km (just above the boundary layer) to 13 km (near the tropopause), with the largest values (1.5 m^2 sec^{-2} per analysis standard deviation) generally between 4-12 km.

At longer lead times, the sensitivity patterns for meridional wind and θ_e remain qualitatively similar to the results for the 12-hour MKE forecast. One standard deviation errors in the analysis meridional winds on the east side of the AEW are associated with a 1.8 m^2 sec^{-2} change in the 48 hour MKE, but the sensitivity on the west side of the AEW is statistically insignificant (Fig. 3c). The region of largest sensitivity for mid-tropospheric θ_e (2.0 m^2 sec^{-2} per analysis standard deviation) is on the northwest side of the initial AEW, slightly west of the main region of sensitivity for the 12-hour forecast, but still near the Jos Plateau (Fig. 3d).

The sensitivities to 700 hPa meridional winds suggest that the AEW amplitude forecast has memory of the initial AEW amplitude at short lead times, but not necessarily at longer lead times. To quantify this idea, Fig. 5 shows the ensemble correlation between the 700 hPa MKE forecast at various lead times averaged over a box centered on the ensemble-mean AEW position to the analysis value. The correlation between the forecast and the initial MKE decreases from 0.7 to 0.4 for a 12 and 48 hour forecast, respectively. This result suggests that

the initial AEW amplitude has little impact on the forecast amplitude after one day, and supports the notion that initial condition errors in other fields, such as the thermodynamic profile have a larger impact on two-day forecasts.

Although the initial AEW is stronger, 10Sept is characterized by qualitatively similar patterns of initial condition sensitivity. For 12-hour MKE forecasts, errors in the northerly (southerly) winds on the west (east) side of the AEW over Southern Mali have the largest impact on the MKE forecast (Fig. 3e). Decreasing (increasing) the winds on the west (east) side of the AEW by one standard deviation leads to a 1.5 m^2 sec^{-2} increase in the 12 hour MKE forecast within the box, equivalent to a 0.3 standard deviation change in this metric (see Fig. 2d for location of the AEW). Similar to 8Sept, the MKE is sensitive to mid-tropospheric θ_e on the west side of the AEW in Burkina-Faso [1.8 m^2 sec^{-2} per analysis standard deviation, Fig. 3f].

Vertical profiles within the most sensitive regions support the idea that errors over a deep column can have a large impact on this metric. For meridional winds, the region of statistically significant sensitivity extends from 2-7 km, with the largest sensitivity value (2.0 m^2 sec^{-2} per analysis standard deviation) at 2.5 km, just below the maximum in northerly winds (Fig. 4c). In contrast, the sensitivity to θ_e is statistically significant throughout the troposphere (Fig. 4d). Moreover, the largest sensitivity values (1.8 m^2 sec^{-2} per analysis standard deviation) are between 2 and 6 km, which coincides with the column θ_e minimum.

To further understand the sensitivity to θ_e within this region, the 10Sept 12 hour forecast for the ensemble member with the largest MKE (denoted "strong") is compared to the 12 hour forecast for the ensemble member with the smallest MKE (denoted "weak"). For

the "strong" member, the mid-tropospheric θ_e is up to 3.5 K higher in the most sensitive region (not shown). Fig. 6 shows the vertical profiles of the cumulus parameterization time-mean heating rates and vertical motion averaged over the right half of the box shown in Fig. 3f, which encloses the region of greatest precipitation. For the "strong" member, the heating rate and vertical motion in the mid-troposphere are 40% and 200% greater than the "weak" member. Moreover, the convective available potential energy (CAPE) is similar for both of these members (not shown), which suggests that the higher θ_e in the "strong" member is associated with less dry-air entrainment.

Similar to 8Sept, the 48-hour forecast for 10Sept shows larger sensitivity to the mid-tropospheric θ_e as compared to the meridional winds. Whereas the sensitivity to meridional winds is generally statistically insignificant (Fig 3g), the region of largest sensitivity for θ_e is along the northwest side of the AEW between Burkina Faso and Mali, which is slightly north of the most sensitive region for the 12 hour MKE forecast. (Fig 3h). A one standard deviation error in this region leads to a 2.7 m^2 sec^{-2} change in the 48 hour MKE forecast. Moreover, the correlation between the forecast AEW amplitude and the analysis AEW amplitude is 0.4 (0.1) for a 12 (48) hour forecast (Fig. 5). Although Park and Droegemeier (2000) studied an individual supercell, their results also indicate a greater sensitivity to the initial errors in the potential temperature and moisture profiles.

b. AEW Longitude

The remainder of this section considers how initial condition errors impact AEW position forecasts at these two initialization times. For this metric positive (negative) sensitivity indi-

cates that increasing the analysis field at that location is associated with eastward (westward) displacement in the AEW.

For 8Sept, the sensitivity results for this metric shows close similarity with the MKE forecast sensitivity pattern. Specifically, the region of largest sensitivity for meridional winds (1° per analysis standard deviation) is associated with the initial AEW and appears to be a super-position of position and amplitude changes, such that increasing the winds associated with the AEW, or shifting the AEW to the east is associated with less westward motion (Fig. 7a). For θ_e, initial condition errors on the southeast side of the AEW over southern Nigeria have the greatest impact on longitude forecasts (Fig. 7b). Increasing (decreasing) θ_e in this region by one standard deviation leads to an AEW that is 1.2° to the east (west). Since some of the ensemble member forecasts did not have an AEW beyond 24 hours, it is not possible to compute the initial-condition sensitivities at longer lead times.

Longitude forecasts for 10Sept show consistent sensitivity to the initial conditions at both forecast times. At the 12 hour lead time, errors in the meridional wind gradient at the center of the AEW over Burkina Faso (Fig. 7c) have the greatest impact on position forecasts. Decreasing (increasing) the winds in this region, akin to shifting the AEW to the east, leads to a 0.5° eastward (westward) change in the forecast longitude. For θ_e, the largest sensitivity is along the western side of the AEW along the Burkina Faso-Mali border [0.4° per analysis standard deviation; Fig. 7d]. Longer lead-time forecasts are characterized by similar areas of large sensitivity; one standard deviation errors in either field are associated with a 0.7 deg change in the AEW position (Fig. 7e,f). At all forecast lead times, the forecast longitude is uncorrelated with the analysis longitude, which suggests that errors in the initial AEW position have a minimal impact on the forecast position. Although there is

strong correspondence between the regions of maximum sensitivity for this metric and the MKE (cf. Fig. 3g,h), the correlation between these two metrics (i.e., 12 hour MKE forecast and 12 hour longitude forecast) is less than 0.15 at all forecast hours.

5. Perturbed Initial Conditions

The ensemble-based sensitivity patterns in the previous section indicate that errors in sensitive regions play a significant role in subsequent forecasts of AEW amplitude. This hypothesis is tested here by applying perturbations to the initial conditions in the most sensitive regions, integrating the perturbed ensemble forward and evaluating the impact on the forecast metric. These experiments also provide a quantitative validation of the sensitivity values shown previously.

Perturbed initial conditions for 8Sept and 10Sept are generated as follows. First, a grid point is chosen within the region where the 48-hour MKE forecast is most sensitive to the mid-tropospheric θ_e (shown as a dot in Fig. 3d,h). A perturbed ensemble initial condition for the ith state variable (x_i^p) is generated via

$$\mathbf{x}_i^p = \mathbf{x}_i^a + \frac{\partial x_i^a}{\partial x_s}\alpha, \tag{2}$$

where

$$\frac{\partial x_i^a}{\partial x_s} = \frac{cov(\mathbf{x}_i^a, \mathbf{J})}{var(\mathbf{x}_s)}.$$

Here, $\mathbf{x}_i^a$ and $\mathbf{x}_s$ are $1 \times M$ ensemble estimates of the ith control analysis state variable and

mid-tropospheric θ_e within the most sensitive region, respectively, and α is the perturbation to the analysis θ_e. Similar to (1), $\frac{\partial x_i^a}{\partial x_s}$ represents a linear regression coefficient where the independent variable is a θ_e perturbation and the dependent variable is the initial condition perturbation associated with adjusting the analysis θ_e. The perturbed ensemble is integrated forward 48 hours and the forecast MKE is computed and compared to the control ensemble estimate. This procedure is repeated for various values of α ($\pm$ 3 standard deviations of $\mathbf{x}_s$) to determine the valid range of sensitivity values and the range over which the model is linear.

Figure 8 shows the response of 48 hour MKE forecasts to perturbations in θ_e as a function of amplitude. For 8Sept, there is generally good agreement between the ensemble prediction and model response for perturbations up to 1 K, while larger amplitude initial-condition perturbations show an asymmetric response with respect to α. The model response to large negative (positive) perturbations is generally less (greater) than the ensemble prediction and the ensemble variance is smaller (larger). Whereas the negative perturbation results are due to MKE being bounded from below by zero, the results for positive perturbations suggest a non-linear amplification. Perturbations applied to 10Sept show better agreement between the ensemble prediction and model response (Fig. 8b), which lends confidence to the hypothesis that errors in the θ_e profile downstream have a large impact on the subsequent AEW amplitude forecast.

The above process is repeated for both 8Sept and 10Sept, except now the 700 hPa meridional wind is perturbed within the most sensitive region for the respective 12 hour MKE forecast (denoted by dots in Fig. 3a,e) and the ensemble is integrated forward 12 hours[1].

[1]12 hour forecasts are used here since the ensemble-based sensitivities are generally statistically insignif-

For 8Sept, the results indicate good agreement between the model response and ensemble prediction for meridional wind perturbations between -7 m $\sec^{-1}$ and 2 m $\sec^{-1}$ (Fig. 8c). At large α, the model response is less than the ensemble prediction, possibly due to MKE having a lower bound. In contrast, 10Sept shows good agreement over all values of α (Fig. 8d).

Finally, perturbations are applied to the mid-tropospheric θ_e and 700 hPa meridional winds in the most sensitive region for the 10Sept 48 hour AEW longitude forecast (denoted by dots in Fig. 7d,f) using the above procedure. Fig. 9a shows that the response of 48 hour AEW longitude forecasts is qualitatively similar to the ensemble prediction of the impact of θ_e and meridional wind perturbations over most of this range of values. There is a slight asymmetry whereby positive perturbations in θ_e (meridional wind) yield position differences that are greater (smaller) than the ensemble prediction.

6. Sensitivity to Cumulus Parameterization

Given that moist dynamics play an important role in AEW dynamics and that a majority of precipitation is generated by the Kain Fritsch (KF) cumulus parameterization, it is possible that the initial-condition sensitivity to mid-tropospheric θ_e is particular to the formulation of the Kain-Fritsch scheme. To test this possibility, two sets of 96 member ensemble forecasts are generated from the 10Sept analysis ensemble. One set of ensemble forecasts use the Betts Miller-Janjic (BMJ) cumulus scheme (Janjic 1994), and the second set of forecasts use the Grell-Devenji cumulus scheme (Grell and Devenyi 2002); all other model settings are kept the same, including the initial conditions. From each set of ensemble forecasts, the MKE

icant beyond this lead time

and AEW longitude metrics are calculated and the initial-condition sensitivity is evaluated.

Probability density functions (PDF) of the MKE and longitude forecasts from these three sets of ensemble forecasts show significant variability arising from using different cumulus parameterizations (Fig. 10). For the 12 hour MKE forecast, the PDF for the KF and Grell ensembles peak at 18 m^2 sec^{-2} and have a longer positive tail, while the peak in the BMJ ensemble is 1.5 standard deviations greater than the other two (Fig 10a). The peak in the 12-hour AEW longitude PDF is at a similar location for all cumulus schemes, though the Grell (BMJ) is furthest west (east) [Fig. 10b]. At the 48 hour lead time, the peak in the KF and Grell MKE ensemble is at 28 m^2 sec^{-2}, compared to 18 m^2 sec^{-2} for the BMJ ensemble (Fig 10c). Longitude forecasts show significant variability among methods, with the Grell (BMJ) peaking at 11 °W (8 °W). The forecast PDF differences show that model formulation errors can also have a large impact on AEW position forecasts.

Figure 11 shows that the 12 hour MKE forecast sensitivity is similar for all three cumulus scheme forecasts; however, the same is not necessarily true at the 48 hour lead time. For 12 hour forecasts, the largest sensitivity for the MYJ and Grell MKE forecasts is in western Burkina-Faso, which is similar to the results for the KF forecast (c.f. Fig. 3g). One standard deviation errors in the mid-tropospheric θ_e near the AEW are associated with a 1.3 (1.8) m^2 sec^{-2} change in the 12 hour MKE forecast that employs the BMJ (Grell) scheme (Fig 11a-b). For 48 hour forecasts, the BMJ shows more sensitivity to the θ_e on the eastern side of the AEW (Fig. 11d), while the region of high sensitivity for the Grell ensemble is on the downstream side of the AEW (Fig. 11e), which is qualitatively similar to the KF results (c.f. Fig 3h). The consistent sensitivity for the KF and Grell schemes suggest that these techniques have a greater memory of initial condition errors as compared to BMJ.

In contrast to MKE, the initial-condition sensitivity for AEW longitude demonstrates more consistency among the various cumulus parameterization schemes. 12 hour AEW longitude forecasts are most sensitive to the θ_e on the west side of the AEW; increasing θ_e by one standard deviation errors leads to a forecast AEW that is 0.4 ° to the west (Fig. 12a-b); this area is similar to the main region of sensitivity for KF forecasts (cf. Fig. 7e). For 48 hour longitude forecasts, the most sensitive region remains along the western side of the AEW. One standard deviation errors in this region have the largest (smallest) impact on the KF (BMJ) longitude forecast.

Finally, high-resolution, two-way nested ensemble forecasts initialized from the 10Sept analysis ensemble are generated to explore the possibility that forecasts with explicit convection will have a different initial-condition sensitivity. The two nested domains are shown in Fig. 1 and have 12 km and 4 km horizontal grid spacing, respectively. All other model settings are the same as the control ensemble, except that the innermost nest does not employ a cumulus parameterization. For consistency with the previous results, both forecast metrics are computed from the 36 km domain output. For grid points that overlap with the 4 km domain, the 36 km forecast is given by the horizontal average of the 4 km forecast. While the explicit MKE forecast PDF is similar to the KF forecast PDF at both lead times (Fig. 10a,c), the ensemble with explicit convection propagates faster (Fig. 10b,d).

Initial-condition sensitivities computed from the explicit convection forecasts show qualitatively similar results to the convection parameterization forecasts. 12 hour MKE and AEW longitude forecasts are sensitive to the θ_e on the west side of the AEW; one standard deviation errors are associated with a 1.8 m^2 sec^{-2} and 0.4 ° longitude differences, respectively, which is similar to the sensitivity results for all cumulus parameterization schemes (Fig. 11c,

12c). At longer lead times the explicit forecast initial-condition sensitivities are qualitatively similar to the KF forecast results. Increasing (decreasing) the θ_e on the west side of the AEW by one standard deviation is associated with a 2.0 m^2 sec^{-2} increase (decrease) in the 48-hour MKE and a 0.7° westward (eastward) displacement in the AEW position, respectively (Fig. 11f,12f).

7. Summary and Conclusions

This manuscript describes the sensitivity of forecasts of a strong AEW to the initial conditions using data drawn from a cycling EnKF system coupled to the WRF model. This EnKF system assimilates conventional in situ observations from surface stations, rawinsondes, ACARS and cloud motion vectors each six hours. At two different analysis times representing different points in the AEW's lifecycle, all 96 ensemble members are integrated forward 48 hours to provide a sample for initial condition sensitivity calculations. Whereas the 8Sept ensemble forecasts show significant variability among ensemble members possibly due to the lack of data near the AEW, the 10Sept forecasts are characterized by less variability.

The sensitivity of AEW amplitude and position forecasts to the initial conditions is determined via ensemble analysis and forecast data using ensemble-based sensitivity analysis. Short lead time forecasts of the meridional wind kinetic energy, which is used as a proxy for AEW amplitude, are most sensitive to the meridional winds within the analysis AEW and to the thermodynamic profile near the AEW, such that a stronger AEW, or higher θ_e above the boundary layer leads to a stronger forecast AEW. In contrast, longer lead-time

forecasts ($>$ 24 hours) are more sensitive to errors in the θ_e field as compared to errors in the meridional wind field. For 10Sept (8Sept) longitude forecasts, errors in the initial θ_e downstream (upstream) of the AEW are associated with the largest forecast differences.

These results indicate that moist processes associated with the cumulus parameterization are dominant at long lead times, which results from moist instability errors that ultimately limit the predictability of larger-scale features (e.g., Zhang et al. 2003). As a consequence, it is more important to constrain analysis errors in the initial temperature and moisture fields near the AEW, rather than the wind field. Forecasts in this region may benefit from temperature and moisture observations, such as from extra rawinsondes, or Global Positioning System (GPS) refractivity profiles (e.g. Anthes et al. 2008), as compared to extra wind data. Tompkins et al. (2005) reached a similar conclusion using the ECMWF 4D-Var system. In addition, the sensitivity to θ_e over the Jos Plateau suggests that initial condition errors over elevated terrain may also play a significant role in AEW forecasts; this idea will be explored in future research.

Diagnostic perturbations in the most sensitive regions are added to the initial conditions based on ensemble sensitivity to confirm the relationship between initial θ_e errors and AEW forecasts. For small perturbations to the meridional wind and θ_e, the forecast difference from non-linear model integrations compare favorably with the ensemble prediction of how perturbing these fields impacts MKE and AEW longitude forecasts. For large positive θ_e perturbations, the model response can be greater than the ensemble prediction, which suggests that positive errors lead to non-linear amplification.

Sensitivities are computed for ensemble forecasts that use the same set of initial conditions, but different cumulus parameterizations and a nested ensemble forecast which uses

explicit convection. Whereas the ensemble forecasts using the KF, Grell and explicit convection showed similar AEW amplitude and position PDFs, the BMJ was more than one standard deviation different, which indicates that model errors associated with the cumulus scheme can be just as important as initial-condition errors. At short lead times, the initial-condition sensitivity for AEW amplitude forecasts are similar regardless of cumulus parameterization scheme. Whereas the 48 hour AEW amplitude forecast with the KF scheme and explicit convection show consistent sensitivity to errors in the θ_e field, BMJ shows less initial-condition sensitivity at longer lead times. In contrast, ensemble position forecasts using all schemes show consistent regions of sensitivity at all forecast hours, even though the AEW ends up at a different position for each cumulus scheme.

Acknowledgments.

A portion of this work was done as a post-doctoral fellow in the NCAR Advanced Study Program, whose support is greatly appreciated. I would like to thank Jeff Anderson (NCAR), Gareth Berry (U. Albany), Chris Snyder (NCAR), Chris Thorncroft (U. Albany), and Morris Weisman (NCAR) for providing feedback on this work. Nancy Collins and Kevin Raeder provided support on using the WRF-DART system. I would also like to acknowledge the high performance computing support provided by NCAR's Computational and Information Systems Laboratory, sponsored by the National Science Foundation.

REFERENCES

Ancell, B. and G. J. Hakim, 2007: Comparing adjoint and ensemble sensitivity analysis. *Mon. Wea. Rev.*, **135**, 4117–4134.

Anderson, J., T. Hoar, K. Raeder, H. Liu, N. Collins, R. Torn, and A. Arellano, 2008: The data assimilation research testbed: A community data assimilation facility. *Bull. Amer. Meteor. Soc.*, **89**, In Review.

Anderson, J. L., 2001: An ensemble adjustment Kalman filter for data assimilation. *Mon. Wea. Rev.*, **129**, 2884–2903.

Anderson, J. L., 2008: Spatially-varying adaptive covariance inflation for an ensemble filter. *Tellus*, **60A**, In Review.

Anthes, R. A., et al., 2008: The COSMIC/FORMOSAT-3 Mission: Early results. *Bull. Amer. Meteor. Soc.*, **89**, 313–333.

Arnault, J. and F. Roux, 2008: Case-study of a developing African easterly wave: An energetic point of view. *J. Atmos. Sci.*, **65**, Submitted.

Avila, L. A. and R. J. Pasch, 1992: Atlantic tropical systems of 1991. *Mon. Wea. Rev.*, **120**, 2688–2696.

Berry, G. J. and C. Thorncroft, 2005: Case study of an intense African easterly wave. *Mon. Wea. Rev.*, **133**, 752–766.

Berry, G. J., C. Thorncroft, A. Agusti-Panareda, J. Heming, J.-P. Lafore, and W. Thiaw, 2008: Intercomparison of African easterly wave representation in operational numerical weather prediction models. *Wea. Forecasting*, Submitted.

Berry, G. J., C. Thorncroft, and T. Hewson, 2007: African Easterly Waves during 2004 - Analysis using objective techniques. *Mon. Wea. Rev.*, **135**, 1251–1267.

Brown, D. P., 2006: Hurricane Helene Tropical Cyclone Report. Tech. Rep. AL082006, National Hurricane Center, 13 pp. pp., Miami, FL.

Burpee, R. W., 1972: The origin and structure of easterly waves in the lower troposphere of North Africa. *J. Atmos. Sci.*, **29**, 77–90.

Fink, A. H. and A. Reiner, 2003: Spatio-temporal variability of the relation between African easterly waves and West African squall lines in 1998 and 1999. *J. Geophys. Res.*, **108**, 4332.

Gaspari, G. and S. E. Cohn, 1999: Construction of correlation functions in two and three dimensions. *Quart. J. Roy. Met. Soc.*, **125**, 723–757.

Grell, G. A. and D. Devenyi, 2002: A generalized approach to parameterizing convection combining ensemble and data assimilation techniques. *Geophys. Res. Lett.*, **29**, 1693.

Hakim, G. J. and R. D. Torn, 2008: Ensemble synoptic analysis. *Fred Sanders Monograph*, L. F. Bosart and H. B. Bluestein, Eds., American Meteorological Society, In press.

Hong, S. Y., J. Dudhia, and S. H. Chen, 2004: A revised approach to ice microphysical

processes for the bulk parameterization of clouds and precipitation. *Mon. Wea. Rev.*, **132**, 103–120.

Hong, S.-Y., Y. Noh, and J. Dudhia, 2006: A new vertical diffusion package with an explicit treatment of entrainment processes. *Mon. Wea. Rev.*, **134**, 2318–2341.

Hsieh, J.-S. and K. H. Cook, 2007: A study of the energetics of African easterly waves using a regional climate model. *J. Atmos. Sci.*, **64**, 421–440.

Janjic, Z. I., 1994: The step-mountain eta coordinate model: further developments of the convection, viscous sublayer and turbulence closure schemes. *Mon. Wea. Rev.*, **122**, 927–945.

Kain, J. S. and J. M. Fritsch, 1990: A one-dimensional entraining detraining plume model and its application in convective parameterization. *J. Atmos. Sci.*, **47**, 2784–2802.

Park, S. K. and K. K. Droegemeier, 2000: Sensitivity analysis of a 3D convective storm: Implications for variational data assimilation and forecast error. *Mon. Wea. Rev.*, **128**, 140–159.

Payne, S. W. and M. M. McGarry, 1977: The relationship of satellite inferred convective activity to easterly waves over west Africa and the adjacent ocean during phase III of GATE. *Mon. Wea. Rev.*, **105**, 413–420.

Redelsperger, J. L., C. D. Thorncroft, A. Diedhiou, T. Lebel, D. J. Parker, and J. Polcher, 2006: African Monsoon Multidisciplinary Analysis: An international research project and field campaign. *Bull. Amer. Meteor. Soc.*, **87**, 1739–1746.

Reed, R. J., D. C. Norquist, and E. E. Recker, 1977: The structure and properties of African wave disturbances as observed during phase III of GATE. *Mon. Wea. Rev.*, **105**, 317–333.

Skamarock, W. C., J. B. Klemp, J. Dudhia, D. O. Gill, D. M. Barker, W. Wang, and J. G. Powers, 2005: A description of the Advanced Research WRF Version 2. Tech. Rep. 468+STR, National Center for Atmospheric Research, 88 pp. pp., Boulder, CO.

Thorncroft, C. D. and B. J. Hoskins, 1994: An idealized study of African easterly waves. Part I: A linear view. *Quart. J. Roy. Met. Soc.*, **120**, 953–982.

Thorncroft, C. D., J.-P. Lafore, G. Berry, R. Roca, F. Guichard, M. Tomasini, and A. N., 2007: Overview of Africa weather systems during the summer of 2006. *CLIVAR Ex.*, **12 (2)**, 18–20.

Tompkins, A. M., A. Diongue-Niang, D. J. Parker, and C. D. Thorncroft, 2005: The African easterly jet in the ECMWF Integrated Forecast System: 4D-Var analysis. *Quart. J. Roy. Met. Soc.*, **133**, 2861–2885.

Torn, R. D. and G. J. Hakim, 2008a: Ensemble-based sensitivity analysis. *Mon. Wea. Rev.*, **136**, 663–677.

Torn, R. D. and G. J. Hakim, 2008b: Ensemble data assimilation applied to RAINEX observations of Hurricane Katrina (2005). *Mon. Wea. Rev.*, Submitted.

Velden, C., et al., 2005: Recent innovations in deriving tropospheric winds from meteorological satellites. *Bull. Amer. Meteor. Soc.*, **86**, 205–223.

Wilks, D. S., 2005: *Statistical Methods in the Atmospheric Sciences*. Elsevier Academic Press, 648 pp.

Zhang, F., C. Snyder, and R. Rotunno, 2003: Effects of moist convection on mesoscale predictability. *J. Atmos. Sci.*, **60**, 1173–1185.

List of Figures

7 Sensitivity patterns for 12-hour AEW longitude forecast to the analysis of (a) 700 hPa meridional wind and (b) 3000-7000 m θ_e (shading, units °) for the forecast initialized 0000 UTC 8 September 2006. The contours are the ensemble-mean analysis field (m $\sec^{-1}$ and K, respectively). (c) and (d) as in (a) and (b), but for the 12-hour forecast initialized 0000 UTC 10 September 2006. (e), (f), as in (c), (d), but for the 48-hour forecast initialized 0000 UTC 10 September 2006. The dots in panels e and f denote the location of the initial condition perturbations described in section 5. 37

8 48-hour ensemble mean MKE forecast differences due to perturbing the analysis 3000-7000 m θ_e field within the most sensitive regions (see text for perturbation location) as determined by integrations of the WRF model (ordinate) against the differences predicted by ensemble sensitivity analysis (abscissa) for forecasts initialized on (a) 0000 UTC 8 September 2006 and (b) 0000 UTC 10 September 2006. The solid line indicates perfect agreement between the predicted response and WRF model integrations, while the error bars denote one ensemble standard deviation. (c) and (d), as in (a) and (b), but for 12-hour ensemble mean MKE differences due to perturbing the 700 hPa analysis meridional wind within the most sensitive region. 38

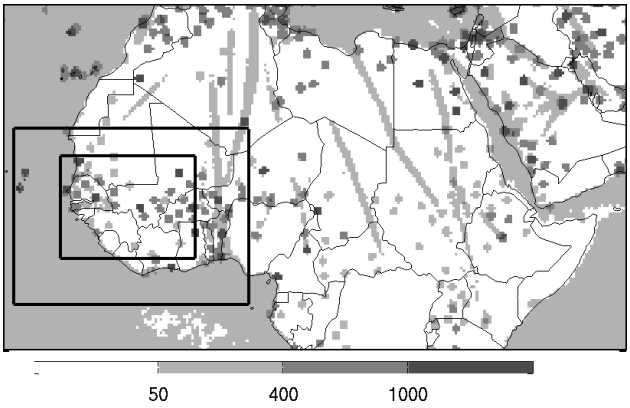

FIG. 1. Total number of observations assimilated by the EnKF system from 0000 UTC 1 September 2006 to 0000 UTC 1 October 2006 (shading). The outer (inner) box denotes the extent of the 12 (4) km domain for the nested ensemble forecasts described in section 6

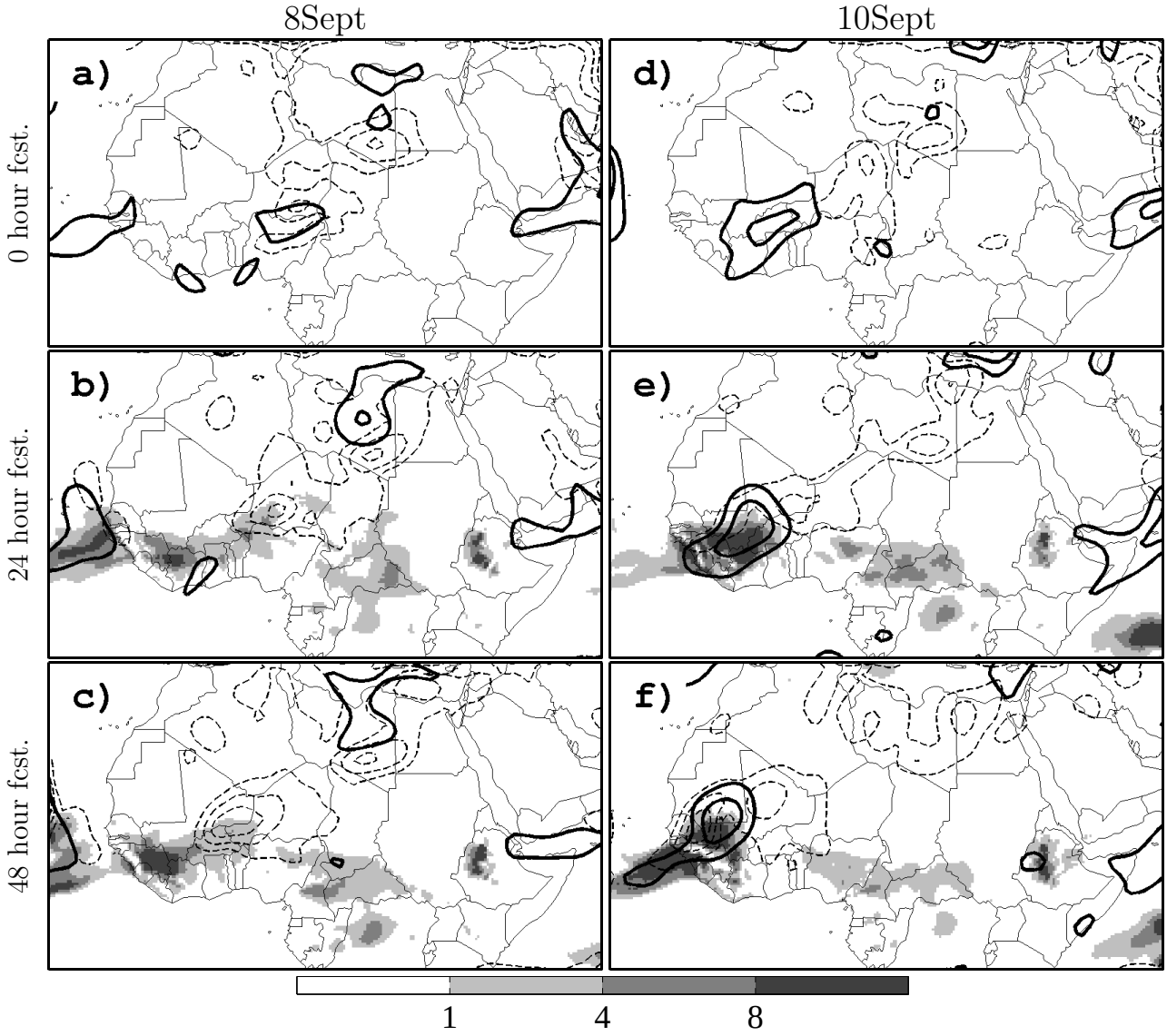

FIG. 2. WRF EnKF (a) 00-hour, (b) 24-hour, and (c) 48-hour ensemble-mean (thick solid lines each 10^{-5} sec^{-1}) and ensemble standard deviation (dashed lines each 0.2×10^{-5} sec^{-1} above 0.5×10^{-5} sec^{-1}) 700 hPa curvature vorticity forecast initialized 0000 UTC 8 September 2006. The shading denotes the WRF EnKF ensemble mean precipitation during the previous six hours (mm per six hours). (d), (e), and (f) as in (a), (b), and (c), but for the forecast initialized 0000 UTC 10 September 2006.

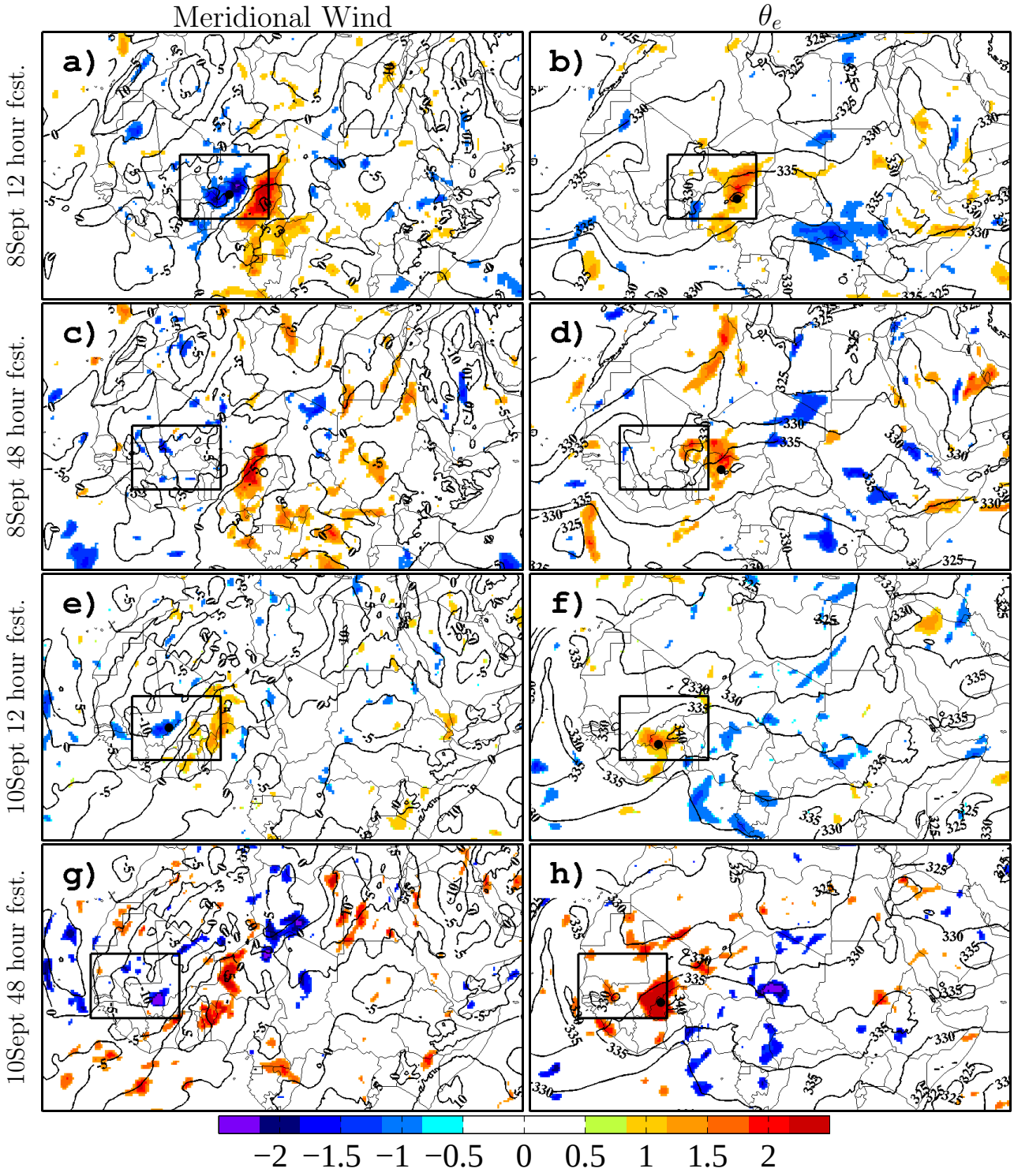

FIG. 3. Sensitivity patterns for 12-hour 700 hPa meridional wind kinetic energy forecast averaged over the box to the analysis of (a) 700 hPa meridional wind and (b) 3000-7000 m θ_e (shading, units m^2 sec^{-2}) for the forecast initialized 0000 UTC 8 September 2006. The contours are the ensemble-mean analysis field (m sec^{-1} and K, respectively). (c) and (d) as in (a) and (b), but for the 48-hour forecast. (e), (f), (g), (h) as in (a), (b), (c), (d), but for the forecast initialized 0000 UTC 10 September 2006. The dots denote the location of vertical sensitivity profiles and initial condition perturbations described in section 5.

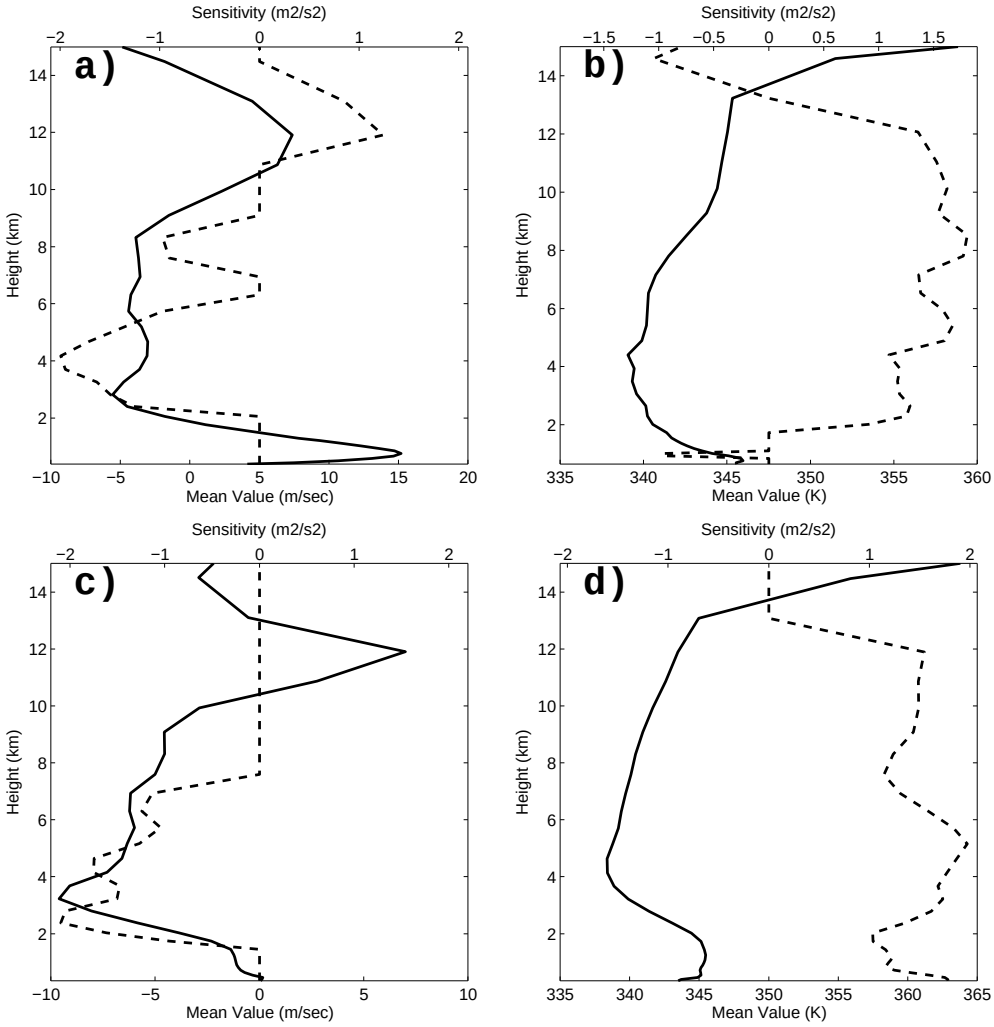

FIG. 4. Sensitivity of 12-hour 700 hPa meridional wind kinetic energy forecast averaged over the box in Fig. 3a to the analysis of meridional wind (dashed line) at the dot in Fig. 3a (abscissa along the top of panel) for the forecast initialized 0000 UTC 8 September 2006. The solid line is the ensemble-mean profile at that horizontal location (abscissa along the bottom of panel). (b), as in (a), but for the analysis of θ_e at the dot in Fig. 3b. (c) and (d), as in (a) and (b), but for the forecast initialized 0000 UTC 10 September 2008. The profile locations are shown in Fig. 3e,f.

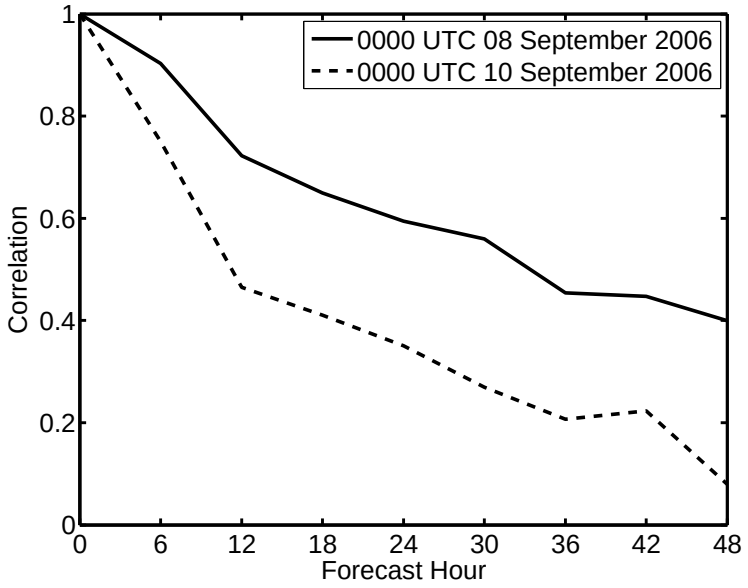

FIG. 5. Correlation of WRF EnKF 700 hPa merdional wind kinetic energy forecast averaged over a 1200 km square box centered on the ensemble-mean AEW to the analysis value as a function of forecast hour. The forecasts are initialized on 0000 UTC 8 September 2006 (solid line) and 0000 UTC 10 September 2006 (dashed line).

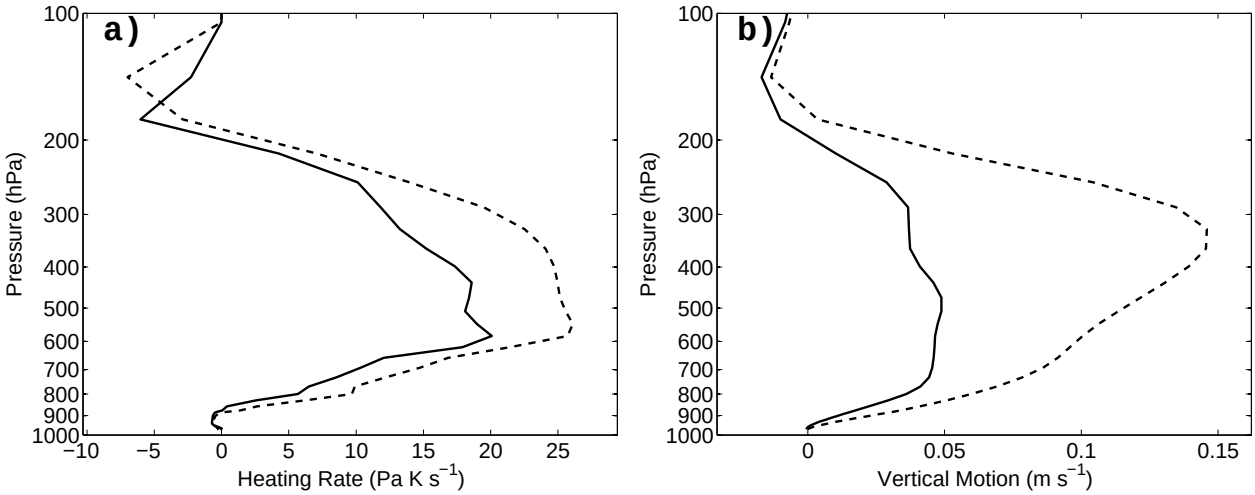

FIG. 6. Vertical profile of the 12-hour time-mean (a) heating profile due to cumulus scheme, and (b) cumulus scheme vertical motion averaged over the right half of the box shown in Fig. 3e for the "weak" (solid line) and "strong" ensemble member (dashed line) forecast initialized 0000 UTC 10 September 2006.

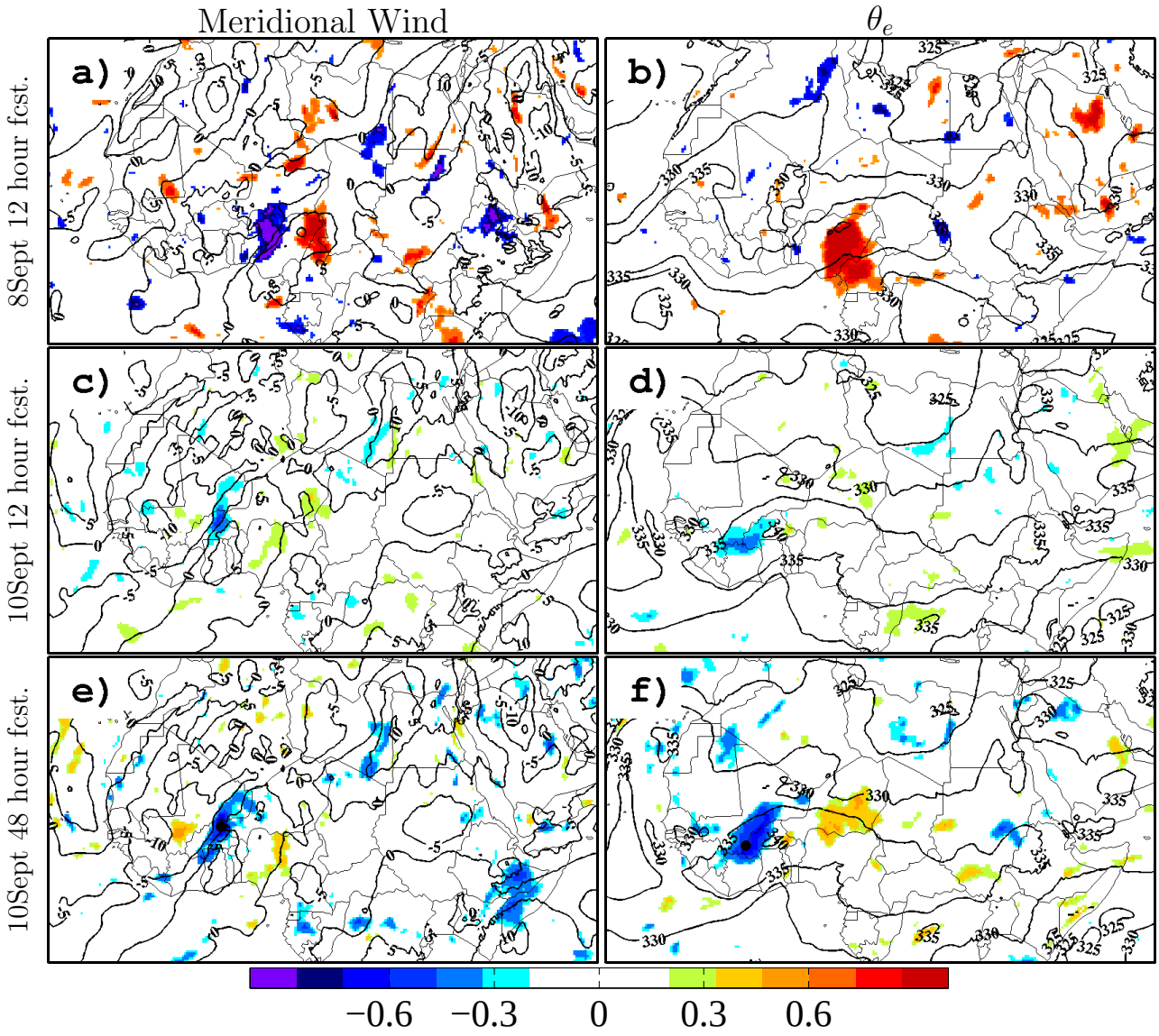

FIG. 7. Sensitivity patterns for 12-hour AEW longitude forecast to the analysis of (a) 700 hPa meridional wind and (b) 3000-7000 m θ_e (shading, units °) for the forecast initialized 0000 UTC 8 September 2006. The contours are the ensemble-mean analysis field (m sec^{-1} and K, respectively). (c) and (d) as in (a) and (b), but for the 12-hour forecast initialized 0000 UTC 10 September 2006. (e), (f), as in (c), (d), but for the 48-hour forecast initialized 0000 UTC 10 September 2006. The dots in panels e and f denote the location of the initial condition perturbations described in section 5.

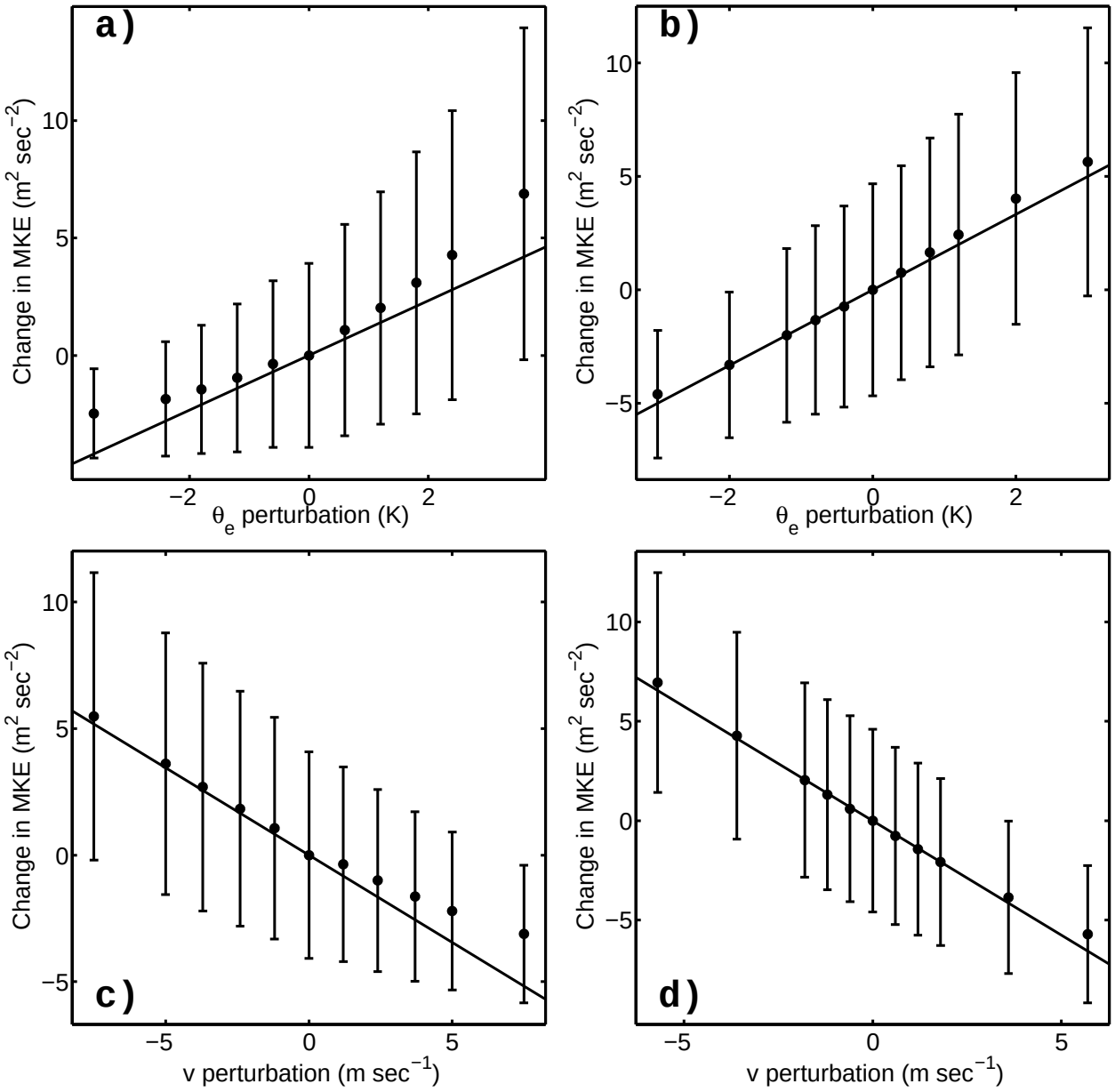

FIG. 8. 48-hour ensemble mean MKE forecast differences due to perturbing the analysis 3000-7000 m θ_e field within the most sensitive regions (see text for perturbation location) as determined by integrations of the WRF model (ordinate) against the differences predicted by ensemble sensitivity analysis (abscissa) for forecasts initialized on (a) 0000 UTC 8 September 2006 and (b) 0000 UTC 10 September 2006. The solid line indicates perfect agreement between the predicted response and WRF model integrations, while the error bars denote one ensemble standard deviation. (c) and (d), as in (a) and (b), but for 12-hour ensemble mean MKE differences due to perturbing the 700 hPa analysis meridional wind within the most sensitive region.

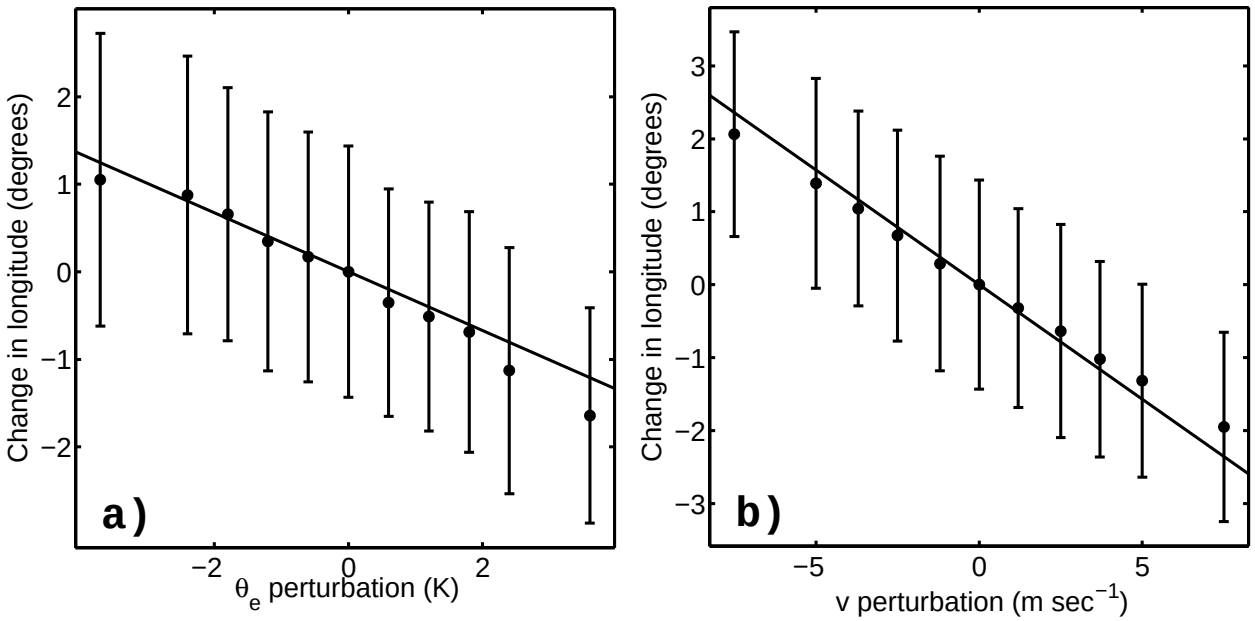

FIG. 9. 48-hour ensemble mean AEW longitude forecast differences due to perturbing the (a) analysis 3000-7000 m θ_e, and (b) 700 hPa merdional wind field within the most sensitive regions (see text for perturbation location) as determined by integrations of the WRF model (ordinate) against the differences predicted by ensemble sensitivity analysis (abscissa) for the forecast initialized 0000 UTC 10 September 2006. The solid line indicates perfect agreement between the predicted response and WRF model integrations, while the error bars denote one ensemble standard deviation.

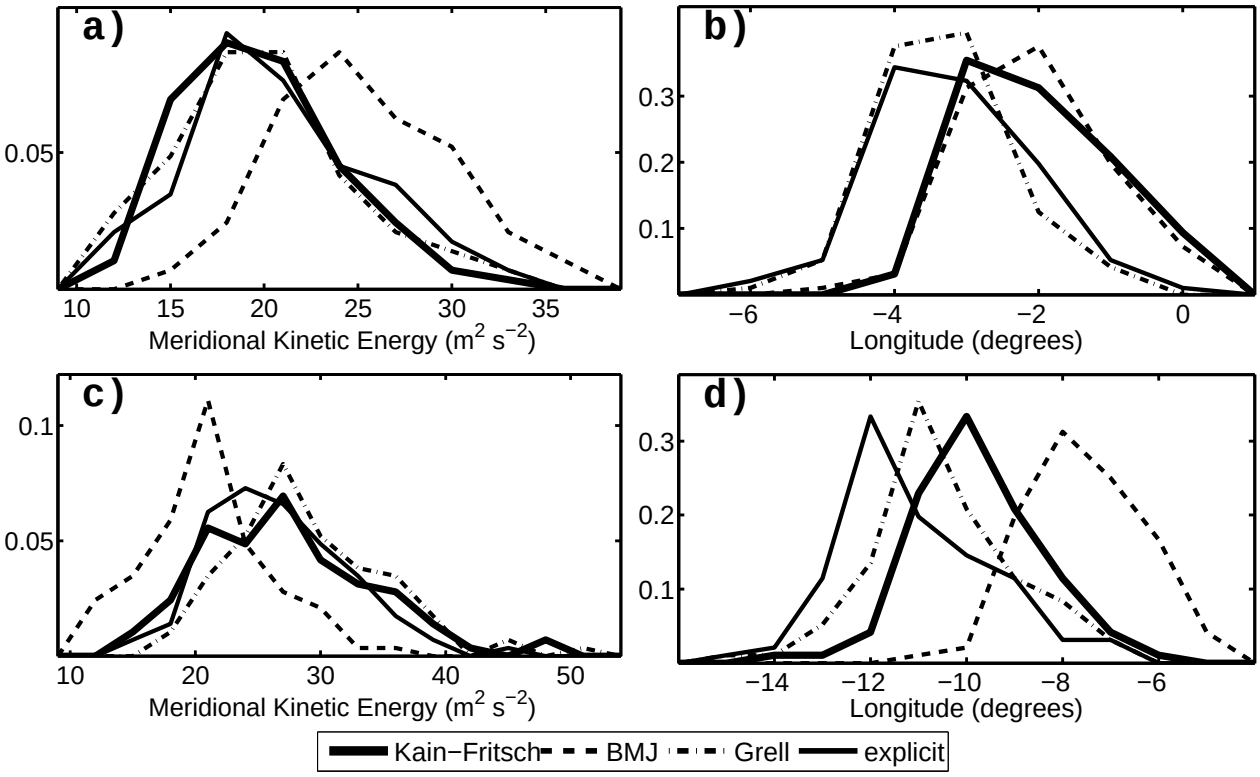

FIG. 10. PDFs of the (a) 12 hour 700 hPa meridional wind kinetic energy and (b) AEW longitude forecast as determined from ensemble forecasts that use KF cumulus scheme (thick solid line), BMJ (dashed line), Grell (dot-dashed line) and explicit convection (thin solid) initialized 0000 UTC 10 September 2006. (c) and (d), as in (a) and (b), but for 48 hour forecasts initialized at the same time.

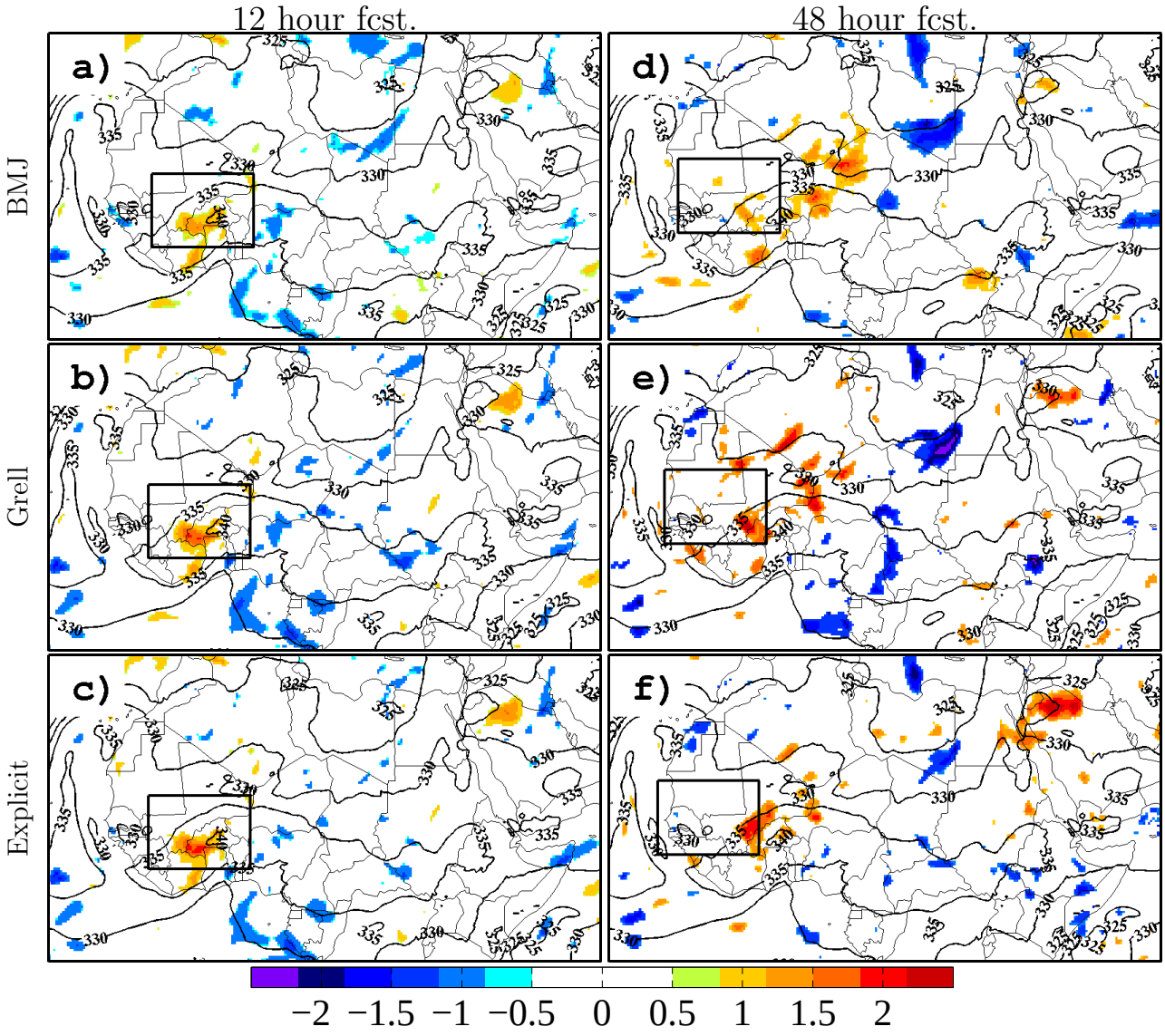

FIG. 11. Sensitivity of 12-hour 700 hPa meridional wind kinetic energy forecast averaged over the box for the (a) BMJ (b) Grell, and (c) explicit forecast ensemble to the analysis of 3000-7000 m θ_e (shading, units m^2 sec^{-2}) initialized 0000 UTC 10 September 2006. The contours are the ensemble-mean analysis field (units: K). (d), (e) and (f), as in (a), (b), (c), but for the 48 hour forecast.

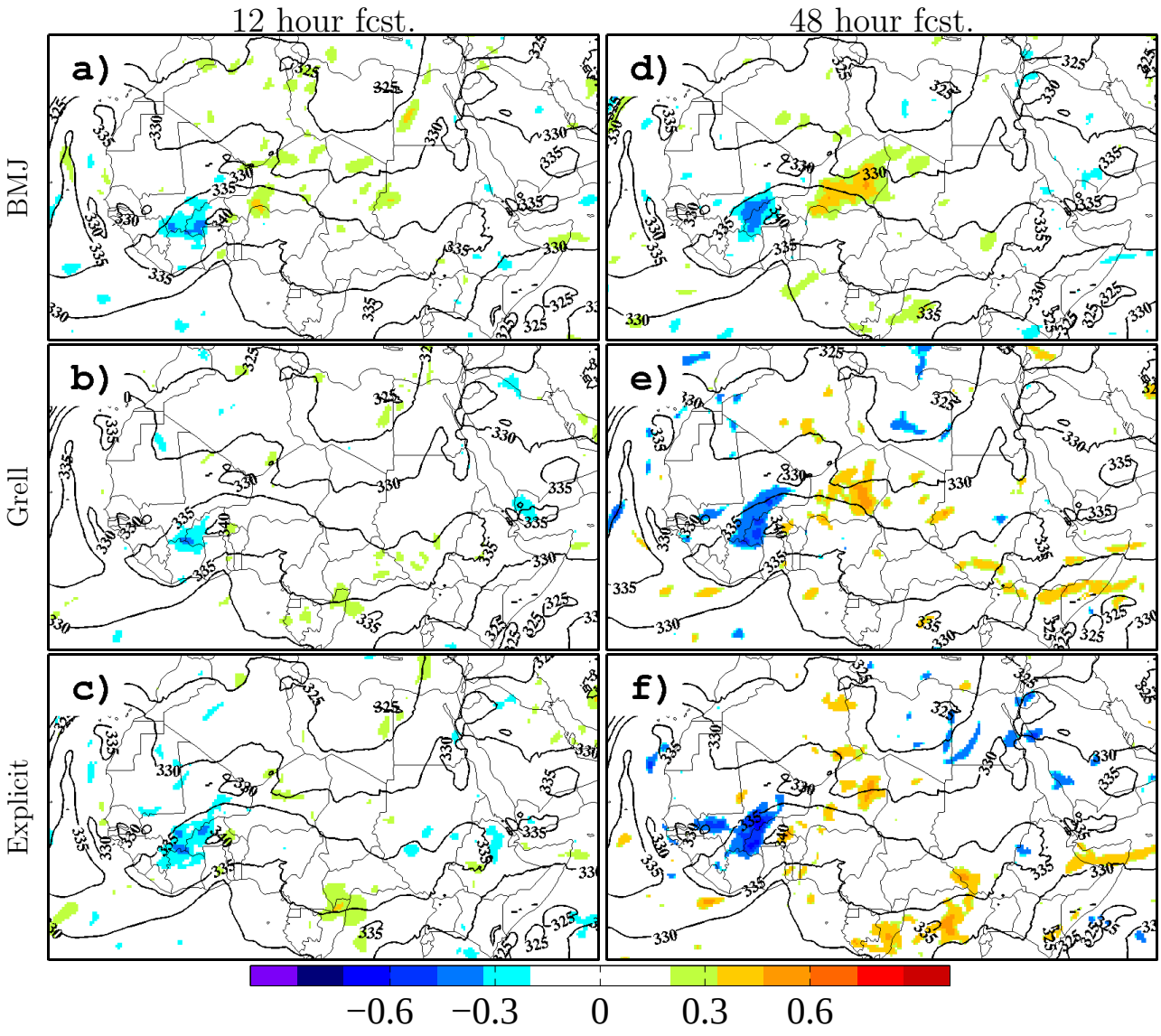

FIG. 12. As in Fig. 11, but for AEW longitude. Units are degrees of longitude.